

Structure of hard-turbulent convection in two dimensions: Numerical evidence

J. Werne

Enrico Fermi Institute, The University of Chicago, Chicago, Illinois 60637

(Received 22 January 1993)

Two-dimensional numerical simulations of a Boussinesq fluid demonstrate the dominant role played by the large-scale circulation in hard-turbulent Rayleigh-Bénard convection. The “roll” coordinates the motions of thermal plumes as they shuttle heat flux directly between the top and bottom boundaries. The roll also subjects the thermal boundary layers to a strong stabilizing shear exhibiting a simple power-law dependence on the Rayleigh number; this power law ($\partial u / \partial z \propto \text{Ra}^{6/7}$) is predicted by a theory [Shraiman and Siggia, *Phys. Rev. A* **42**, 3650 (1990)] which proposes the heat-transport (Nusselt-number) scaling relationship ($\text{Nu} \propto \text{Ra}^{2/7}$) is determined solely by the structure of the thermal and viscous boundary layers. Also, the transition into two-dimensional hard turbulence is observed to coincide with the development of plumes which live sufficiently long to carry heat flux in the “wrong” direction. In addition to these issues of heat transport, the structure of the large-scale roll is investigated and the relationship between the turnover time τ_0 and the coherence frequency ω_p is made precise.

PACS number(s): 47.27.Te, 47.27.Cn, 47.27.Lx, 47.27.Qb

I. INTRODUCTION

In 1987, a “nonclassical” regime of turbulent thermal convection was established by Heslot, Castaing, and Libchaber [1] with the aid of carefully performed high-Rayleigh-number (Ra) experiments in a unit-aspect-ratio Rayleigh-Bénard cell [2]. Subsequent experiments, incorporating both helium and water as working fluids in containers of various sizes and shapes, have aided the characterization of this flow, which has come to be known as “hard turbulence” [3–7].

A distinguishing feature of hard turbulence, as reported in [1], is a significant reduction in the time-averaged heat-transport rate below the “expected” value: Rather than the “expected” scaling of the Nusselt number Nu [8] on the Rayleigh number Ra of $\text{Nu} \propto \text{Ra}^{1/3}$, one finds that above $\text{Ra} \approx 4 \times 10^7$, the heat transport scales as $\text{Nu} \propto \text{Ra}^{2/7}$ [1]. The expected rate is observed, however, in certain situations at lower Ra [9] and an elegant scaling theory exists to describe it [10]. The primary motivation of this paper is to understand what aspects of hard turbulence are essential for restricting the heat flux and reducing the scaling exponent from $\frac{1}{3}$ to $\frac{2}{7}$. We approach this problem by investigating hard turbulence in two dimensions (2D).

Evidence that hard turbulence exists in 2D was first reported in 1990 with the aid of numerical simulations [11]. Noteworthy in [11] is the consistency with the experimental result $\text{Nu} \propto \text{Ra}^{2/7}$ even though the numerical study is conducted in 2D while the experiments are 3D. Subsequent numerical work in 2D [12] reproduces a sufficient number of the defining features of the experimental hard-turbulent state that one is confident the physical mechanism responsible for the Nu scaling with Ra can be understood by investigating the 2D solutions. To this end, this paper serves to outline the dominant features of 2D hard turbulence in an attempt to illuminate the experimental hard-turbulent flow. The pa-

per is organized as follows: Section II provides a short review of the relevant theoretical work on the subject. Section III briefly describes the 2D computer model employed and provides information concerning the spatial resolution of the calculations. The numerical results are described in detail in Sec. IV: In this section, the sequence of bifurcations leading up to the 2D hard-turbulent state are outlined; the important role played by plumes in transporting heat flux through the cell is described; and finally, the structure of the thermal and viscous boundary layers is presented. Section V offers conclusions concerning the theories which attempt to explain the heat-transport scaling relationship in hard turbulence. An appendix is included to detail the structure of the large-scale roll without upsetting the continuity of the rest of the paper, which is primarily concerned with issues of heat transport.

II. HARD-TURBULENCE THEORIES

Several theories have been proposed to explain the heat transport in hard turbulence [4,13–15]. All of these theories successfully derive the scaling relationship $\text{Nu} \propto \text{Ra}^{2/7}$ despite the fact that different theories accentuate different aspects of the flow. Here, we concentrate on the one theory whose approach appears most appropriate in light of the 2D results presented in this paper. This theory is due to Shraiman and Siggia and it suggests that the heat transport is determined solely by the structure of the thermal and viscous boundary layers adjacent to the top and bottom surfaces of the cell [13].

The physical picture of the flow employed by Shraiman and Siggia is one which emphasizes the large-scale roll existing in hard turbulence; this roll produces a mean “wind” along the boundaries and, in so doing, subjects the thermal boundary layers to a strong shear [16]. The strong shear stabilizes the thermal boundary layers, allowing them to be thicker than they would be in the

shear's absence; thicker thermal layers result in a reduced heat-transfer rate. This stabilizing action of the shear was first pointed out by Castaing *et al.* as an explanation of the reduction in the heat transfer from $\text{Nu} \propto \text{Ra}^{1/3}$ to $\text{Ra}^{2/7}$ when the flow undergoes the transition to hard turbulence [4].

Details of the analysis by Shraiman and Siggia include assumptions that (1) the viscous boundary layer has the structure of a turbulent "pipe-flow" profile and (2) the thermal boundary layer is nestled completely within the laminar sublayer of the viscous boundary layer. It is implicitly assumed that the temperature field is passive and plays no role in the fluid motion within the thermal boundary layer. The Nu - Ra scaling relation is obtained by solving the time-independent heat equation in the laminar sublayer and by balancing the total buoyancy work in the cell with the viscous dissipation in the boundary layers. A prediction of this analysis is that the wall stress scales with Ra as follows: $\partial u / \partial z \propto \text{Ra}^{6/7}$ (though this is not pointed out in [13]).

This theory is in marked contrast to the other theories which derive the Nu - Ra scaling relationship in hard turbulence. Those theories [4,14,15] emphasize the heat-transport properties of the turbulent fluctuations in the center of the cell. Shraiman and Siggia, on the other hand, consider only the structure of the boundary layers in deducing the heat transport and suggest that details associated with the fluctuations in the center of the cell do not play an important role.

The 2D results presented below support the basic concept proposed by Shraiman and Siggia: In addition to reflecting the qualitative description of a dominant, large-scale flow and sheared thermal boundary layers, the 2D solutions do indeed exhibit the power law predicted for the wall stress. Despite this agreement, however, the detailed assumptions made in [13] turn out to be unnecessarily restrictive. Indeed, our results discussed below suggest that the scaling results derived by Shraiman and Siggia are more general than is apparent from the detailed calculation presented in [13].

III. TWO-DIMENSIONAL MODEL PROBLEM

Before presenting the 2D solutions, we briefly discuss the numerical model with which the solutions are computed. The model problem incorporates the Boussinesq approximation [17] for an incompressible fluid:

$$\frac{\partial \mathbf{v}}{\partial t} + \boldsymbol{\omega} \times \mathbf{v} = \sigma \nabla^2 \mathbf{v} - \nabla P + \sigma \frac{\mathbf{Ra}}{16} \mathbf{T}, \quad (1)$$

$$\frac{\partial T}{\partial t} + \mathbf{v} \cdot \nabla T = \nabla^2 T, \quad (2)$$

$$\nabla \cdot \mathbf{v} = 0. \quad (3)$$

The vector \mathbf{Ra} is directed vertically upward, opposite to the gravitational force. σ is the Prandtl number of the fluid, ν/κ . The units of length, time, and temperature used to express Eqs. (1)–(3) in their nondimensional form are $L/2$, $L^2/(4\kappa)$, and $\Delta/2$. The variables \mathbf{v} , T , and P are the velocity, temperature, and pressure [18]. $\boldsymbol{\omega}$ is the curl of the velocity field (i.e., the vorticity).

We report here solutions to Eqs. (1)–(3) computed on a square domain of dimensions $L \times L$ using a pseudospectral Fourier-Chebyshev tau method. A description of the numerical algorithm can be found elsewhere [11]; here we mention only those features of the model that are necessary in evaluating the results presented in this paper.

The conditions imposed on the top and bottom boundaries are

$$\mathbf{v}(x, \pm 1) = \mathbf{0}, \quad (1')$$

$$T(x, \pm 1) = \mp 1, \quad (1'')$$

while the boundary conditions on the sidewalls are

$$u(\pm 1, z) = 0, \quad (2')$$

$$\frac{\partial w}{\partial x}(\pm 1, z) = 0, \quad (2'')$$

$$\frac{\partial T}{\partial x}(\pm 1, z) = 0. \quad (2''')$$

Here, (x, z) and (u, w) represent the (horizontal, vertical) components of the coordinates and the velocity, respectively. The unphysical, free-slip-sidewall boundary conditions (2'') are utilized to speed computation [19,20] at the cost of suppressing a backroll instability which occurs in the four corners of the cell [21]. The physical, no-slip conditions (1') are imposed on the top and bottom boundaries to more accurately represent the boundary layers which form there. It will be suggested below that accurate simulation of the thermal and viscous boundary layers on the top and bottom boundaries is crucial in reproducing the $\text{Nu} \propto \text{Ra}^{2/7}$ scaling law.

The spatial and temporal resolution of the numerical runs is evaluated in terms of the Kolmogorov length scale l_K and its associated time scale τ_K [22,23],

$$l_K = (\sigma^3 / \varepsilon)^{1/4}, \quad \tau_K = (\sigma / \varepsilon)^{1/2},$$

where $\varepsilon = \sigma \langle \partial_i \bar{v}_j \partial_i \bar{v}_j + \partial_i \bar{v}_j \partial_j \bar{v}_i \rangle_t$ is the kinetic-energy dissipation rate for the velocity fluctuations. Here, the velocity v_i is decomposed into mean $\langle \langle v_i \rangle_t \rangle$ and fluctuating (\bar{v}_i) components (e.g., $v = \langle v \rangle_t + \bar{v}$) and $\langle \rangle_t$ indicates a temporal average. (Time averaging is employed here, instead of the more customary spatial averaging, because this flow exhibits stationary while it is neither homogeneous nor isotropic; this will become apparent to the reader in later sections.) Note that for steady solutions, $\varepsilon = 0$, $l_K = \infty$, and $\tau_K = \infty$ because ε is defined in terms of the velocity fluctuations \bar{v}_i and not the mean velocity $\langle v_i \rangle_t$.

Adequate spatial resolution of the velocity field is achieved when the grid spacing is sufficiently small to resolve the maximum relevant wave vector k_0 . Typically, this translates into a grid spacing no larger than $\approx 10/l_K$ [e.g., an estimate of k_0 for 3D flows with asymptotically large Reynolds numbers ($\text{Re} = UL/\nu$, where U and L are the velocity and the length scale for the largest-scale features of the flow) is $k_0 l_K = 0.55$ [24]; this gives a grid spacing of $\delta x = 11 l_k$]. Resolving the temperature field is more or less demanding depending on the value of σ . With $\sigma > 1$, the relevant dissipative length scale for the

TABLE I. Spatial and temporal resolution of the numerical simulations. Ra and σ are the Rayleigh numbers and Prandtl numbers for the separate runs. M is the number of grid points in each spatial direction (distributed uniformly in x and nonuniformly in z ; see text). δt is the time step, chosen so that the numerical algorithm is stable. The combination $\sqrt{\sigma}\delta x/l_K$ is the ratio of the grid spacing δx to the dissipative length scale for the fluctuations in the temperature field, $l_K\sigma^{-1/2}$; values of this ratio of 10 or less are interpreted as demonstrating adequate spatial resolution of the small-scale fluctuations. τ_K is the dissipative time scale for the small-scale fluctuations. For the ratio $\delta t/\tau_K < 1$, the calculations resolve τ_K . Note that for steady solutions, $\varepsilon=0$, $l_K = \infty$, and $\tau_K = \infty$ because ε is defined in terms of the velocity fluctuations; see text.

Ra	σ	M	δt	$\sqrt{\sigma}\frac{\delta x}{l_K}$	τ_K	$\frac{\delta t}{\tau_K}$
1.28×10^6	1	97	1.0×10^{-5}	0	∞	0
	7			0.68	8.6×10^{-4}	1.2×10^{-2}
2.56×10^6	1	97	5.0×10^{-6}	0	∞	0
	7			0.81	5.3×10^{-4}	9.4×10^{-3}
5.12×10^6	1	97	3.0×10^{-6}	0	∞	0
	7			1.0	2.8×10^{-4}	1.1×10^{-2}
1.024×10^7	1	129	2.0×10^{-6}	0	∞	0
	7	97	3.0×10^{-6}	1.2	1.6×10^{-4}	1.9×10^{-2}
2.048×10^7	1	129	1.5×10^{-6}	0	∞	0
	7			1.2	8.4×10^{-5}	1.8×10^{-2}
4.096×10^7	1	129	1.0×10^{-6}	0	∞	0
	7			1.5	4.2×10^{-5}	2.4×10^{-2}
8.192×10^7	1	193	2.5×10^{-7}	0	∞	0
	7			1.3	2.5×10^{-5}	1.0×10^{-2}
1.6384×10^8	1	257	2.0×10^{-7}	0	∞	0
	7			1.2	1.5×10^{-5}	1.3×10^{-2}

temperature field is not l_K , but rather $l_K\sigma^{-1/2}$ [25]. Therefore an estimate of the largest acceptable grid spacing with $\sigma \geq 1$ is $\delta x/l_K \approx 10\sigma^{-1/2}$. Our least-resolved run easily satisfies this condition with the instantaneous value of $\delta x/l_K$ (i.e., before time-averaging ε) never exceeding $2.6\sigma^{-1/2}$.

Table I presents information concerning the resolution of the runs. Comparison of the time scale τ_K with the time step δt is straightforward and it is apparent that the time scale for the smallest-scale fluctuations are well resolved by δt for all of the runs. (Stability of the numerical algorithm is the limiting factor in selecting δt [19].) Comparison of the length scale $l_K\sigma^{-1/2}$ with the grid spacing is slightly more involved because the grid points (or collocation points) are distributed uniformly in the horizontal direction, but are located at the positions $z_m = -\cos[m\pi/(M-1)]$ ($m=0, \dots, M-1$), i.e., nonuniformly, in the vertical direction. For this reason, the ratio of the grid spacing δx to the dissipative length scale $l_K\sigma^{-1/2}$ must be considered carefully:

$$\sqrt{\sigma}\frac{\delta x}{l_K} = [(\delta x_i)^4 \langle \partial_i \bar{v}_j \partial_i \bar{v}_j \rangle_t + (\delta x_i)^2 (\delta x_j)^2 \langle \partial_i \bar{v}_j \partial_j \bar{v}_i \rangle_t]^{1/4}.$$

Here, the Einstein summation convention is used for the terms $\partial_i \bar{v}_j \partial_i \bar{v}_j$ and $\partial_i \bar{v}_j \partial_j \bar{v}_i$; the factors δx_i and δx_j are chosen accordingly with $x_1=x$ and $x_2=z$. By defining $\delta x/l_K$ in this way, the grid-spacing direction chosen for each term is aligned with the direction of the gradient for that term.

It is evident from Table I that all of the runs adequately resolve the smallest-scale fluctuations in the temperature and velocity fields. For the steady-state solutions (for which $\varepsilon=0$), spatial resolution must be evaluated in terms of the mean velocity and temperature fields, $\langle v_i \rangle_t$ and $\langle T \rangle_t$, since \bar{v}_i and \bar{T} are both zero. As evidence that the mean fields are adequately resolved we note that both the viscous and thermal boundary layers for all of our solutions are spanned by at least 12 grid spacings.

IV. NUMERICAL RESULTS

A. Transition to 2D hard turbulence

As Ra is increased, the flow undergoes a succession of bifurcations before reaching a turbulent state. Most of these bifurcations occur at critical Ra which depend on σ . Of the two values of σ ($\sigma=1$ and 7) for which we have a complete sets of runs spanning a limited range in Ra ($0 < Ra \leq 1.6384 \times 10^8$), the $\sigma=7$ solutions experience a greater number of bifurcations and reach the 2D hard-turbulent state. Below, we summarize this sequence of bifurcations for $\sigma=7$. We then follow with a brief account of the $\sigma=1$ results which do not attain hard turbulence; we do not yet know if hard turbulence exists in 2D for $\sigma=1$.

The first transition occurs when the purely conductive state ($\mathbf{v}=0$, $Nu=1$) becomes unstable to a steady large-scale roll. The critical Ra , $Ra_c \approx 1700$, is independent of σ and agrees with the linear stability analysis of the conductive state [17]. As Ra is increased further, the roll's

circulation speed increases and the thermal and viscous boundary layers thin. For $\sigma=7$, this steady roll gives way to a periodic state when $Ra = Ra_b \approx 4 \times 10^4$. The resulting periodic state is similar to the “BO2 blob instability” discussed by Bolton, Busse, and Clever [26]: As the flow circulates, two hot and two cold “blobs” travel indefinitely around the cell and are responsible for the periodic time dependence. These blobs are actually the “crests” and “troughs” of two waves which circulate about the center of the cell and completely penetrate the boundary layers; see Fig. 1. The most notable manifestation of these waves are ripples propagating along the thermal boundary layers in the direction of the large-scale flow.

As Ra is increased, the ripples on the boundary layers grow in amplitude, developing into thermal plumes which experience a sizable buoyant force. These plumes compete with the waves in determining the dynamics of the flow. At $Ra \approx 3 \times 10^5$, the plumes are sufficiently large to destabilize the periodic two-wave state described

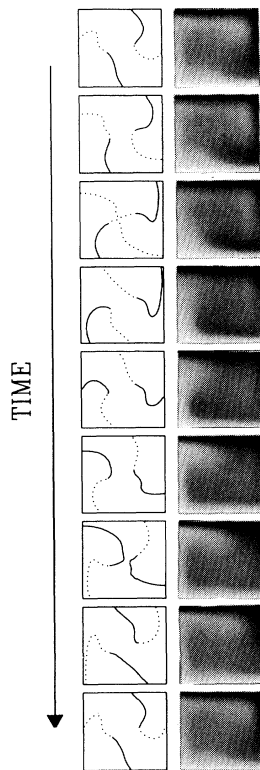


FIG. 1. Periodic convection with $Ra=8 \times 10^4$ and $\sigma=7$. The sequence shows the evolution of the temperature field during one cycle. The right column depicts the temperature field; shades of gray are proportional to the temperature; white represents hot fluid. The left column shows two circulating waves which exist in the flow for this state. Solid lines represent hot “wave crests” while dashed lines depict cold “troughs.” Note the wave-wave interaction occurring in the third and seventh frames. The waves are visualized by plotting $\partial T / \partial t = 0$ contours (i.e., contours of constant phase).

above. The resulting state is chaotic and is characterized by quiescent periods (during which several waves propagate around the cell) that are intermittently disrupted by plumes erupting from the boundary layers. The intermittent plume eruptions dominate the flow, when they occur, and may even reverse the direction of the large-scale roll.

Once $Ra \gtrsim 10^6$, buoyant plumes continually dominate the flow and a description in terms of waves is no longer appropriate; see Fig. 2. Roughly speaking, the plumes emitted from both the top and bottom boundaries become “synchronized” and the direction of the large-scale roll is stabilized: Hot plumes emitted from the bottom boundary travel with the large-scale circulation, impact the top boundary layer and instigate the formation of cold plumes there; these newly formed cold plumes behave similarly and the resulting feedback between the two boundaries is responsible for the stabilization of the roll. This state exhibits some of the properties of the experimental hard-turbulent flow [exponential probability distribution functions (PDF’s) for temperature fluctuations in the center of the cell, scaling of the rms temperature fluctuation Δ_c with $Ra^{-1/7}$, and scaling of the coherence frequency ω_p with $Ra^{1/2}$]; however, most notable is that Nu does not scale with $Ra^{2/7}$ [11,12]. This appearance of some, but not all, of the properties associated with the transition to hard turbulence points out a marked difference between the 2D and 3D flows. This difference is valuable in establishing the features which are, and those which are not, directly linked to the heat-transport scaling observed in hard turbulence.

With $Ra > Ra_T \approx 10^7$ for $\sigma=7$, hard turbulence is obtained; see Fig. 3. The signifying feature of this state is the establishment of $Nu \propto Ra^{2/7}$. Other aspects of the transition include a change in the velocity PDF from Gaussian to exponential form and changes in the scaling exponents for the sidewall velocity and temperature (V_s and T_s) [11,12]. Though the transitions in Nu , V_s and T_s are all abrupt, the change in the velocity PDF is a gradual one spanning roughly one decade in Ra . Through this transition, the temperature PDF in the center of the cell remains exponential and both Δ_c and ω_p maintain their respective power laws with Ra [12]. As will be demonstrated in this paper, this transition is also signaled by a change in the structure of the boundary layers and by the appearance of negative heat flux carried by thermal plumes traveling in the “wrong” direction.

A feature of 2D hard turbulence as Ra is increased above Ra_T is a secondary transition involving the symmetry of the large-scale roll occurring at $Ra \approx 4 \times 10^7$. Such a secondary transition has not been reported for and may not exist in 3D. Aside from a change in symmetry of the roll, the transition is evident through a change in the scaling of ω_p with Ra . ($\omega_p = 2\pi/\tau$, where τ is the “large-eddy” turnover time of the flow; see Fig. 4 and the Appendix.) None of the other features of hard turbulence, including the Nu - Ra scaling, are affected during this second transition.

This secondary transition is easily seen in a plot of the average vertical heat flux $\langle Tw - \partial T / \partial z \rangle_t$ through the mid-height of the cell ($z=0$); see Fig. 5. For $10^7 \leq Ra \leq 4 \times 10^7$, the roll exhibits a left-right asymmetry

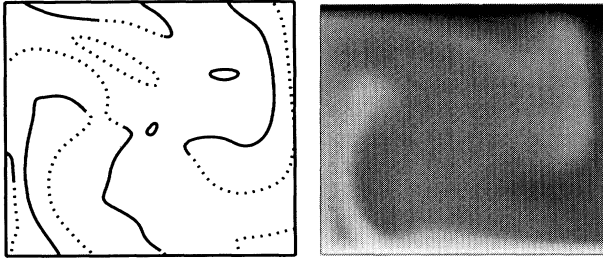


FIG. 2. Plume-dominated convection with $Ra=1.28 \times 10^6$ and $\sigma=7$. As in Fig. 1, on the left are cold (dashed) and hot (solid) $\partial T/\partial t=0$ contours while the temperature field is shown on the right. Thermal plumes grow from the thermal boundary layers and dominate the dynamics of the flow.

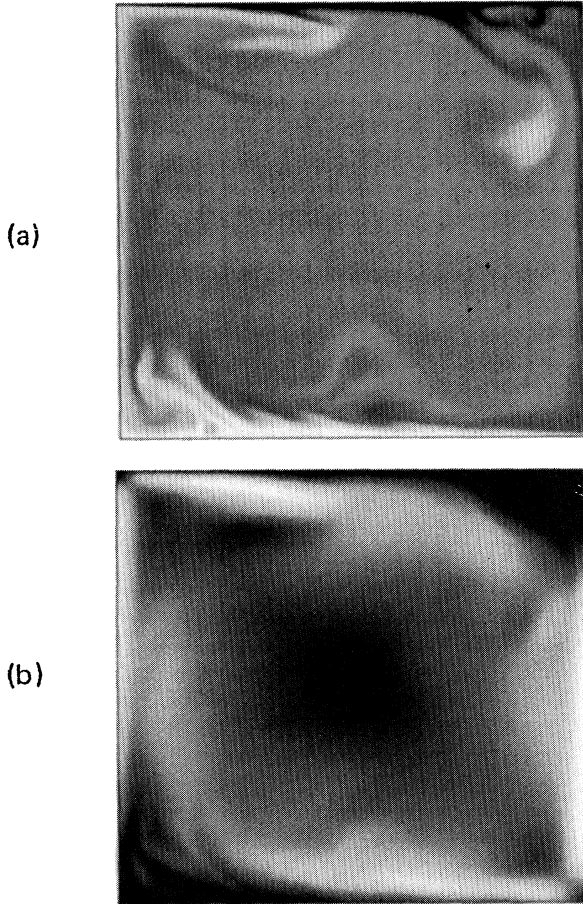


FIG. 3. Hard turbulence. $Ra=1.6384 \times 10^8$ and $\sigma=7$. (a) shows the fluid temperature. (b) depicts the magnitude of the velocity field with white representing high speeds. The maximum velocity for this snapshot is $11\,600(\kappa/L)$. The images relay the plume-roll interplay for hard turbulence: Plumes formed on the boundary layer do so in a strong wind resulting from the large-scale roll. The plumes are swept by the wind downstream where they coalesce to form a large plume. Large hot (cold) plumes, overcome by buoyancy, rise (fall) along the left (right) sidewall, driving the roll. When these large plumes impact the opposite boundary layer, they instigate the formation of other plumes [see top boundary of (a)] which continue the process.

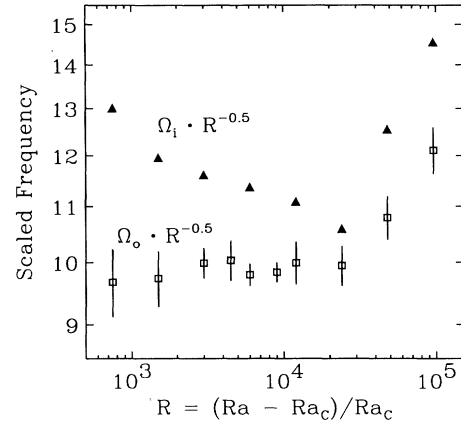


FIG. 4. Coherence frequency scaling with Ra in 2D hard turbulence. Near the outer portion of the large-scale roll (including the boundary layers), $\omega_p = \Omega_o$ scales with Ra with a power-law index of $\frac{1}{2}$ up to $Ra \approx 4 \times 10^7$. At the center of the roll, $\omega_p = \Omega_i$ is higher than Ω_o and exhibits a weaker dependence on Ra for $Ra < 4 \times 10^7$. For $Ra > 4 \times 10^7$, the scaling changes and is indicative of a transition in the symmetry of the large-scale roll. The error bars for Ω_o span the half-width of the peak in the power spectrum. These results are for $\sigma=7$. See the Appendix for a detailed discussion of ω_p .

which is not present for $Ra \geq 8 \times 10^7$, the flux through the ($z=0$) plane being symmetric for $Ra \geq 8 \times 10^7$. The fact that the heat-transport scaling does not reflect this transition at $Ra \approx 4 \times 10^7$ indicates that the transition, as well as a detailed description of the symmetry of the large-scale flow, is more a curiosity of 2D hard turbulence and does not reveal anything crucial to understanding how the heat flux is determined. Indeed, this transition illustrates a feature of hard turbulence (the symmetry of the roll at $z=0$) which develops in a nonuniversal manner despite the algebraic scaling of Nu with Ra . (See the Appendix for a more detailed discussion of the structure of the large-scale roll.)

At this point we remind the reader that the sequence of transitions outlined above, as well as the conclusions already drawn about the heat transport in 2D hard turbulence, pertain to solutions with $\sigma=7$. For $\sigma=1$, the flow develops more slowly as Ra is increased above Ra_c and does not attain hard turbulence for $Ra < 1.6384 \times 10^8$. For example, with $\sigma=1$, the steady-roll state becomes unstable to a time-dependent solution when $Ra = Ra_b \approx 8 \times 10^7$, much higher than the analogous transition at $Ra \approx 4 \times 10^4$ for $\sigma=7$. This increase in Ra_b for decreasing σ is characteristic of the BO2 blob instability [26] and makes low- σ computations more costly: In order to obtain turbulent solutions for $\sigma=1$, higher Ra must be considered than for $\sigma=7$. By $Ra=1.6384 \times 10^8$, the $\sigma=1$ flow is certainly not within the hard-turbulent regime. Figure 6 demonstrate this by presenting a comparison of time traces of T obtained at the position ($x=0.125, z=0$) for $\sigma=1$ and 7. The solution with $\sigma=7$ is well within the hard-turbulent regime; note that its time dependence is chaotic. The solution with $\sigma=1$, on the other hand, appears nearly periodic

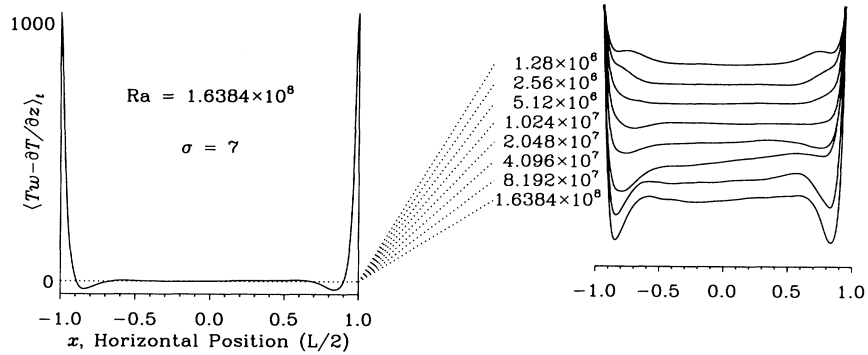


FIG. 5. Vertical heat flux at the cell mid-height ($z=0$) for $\sigma=7$. On the left is the flux for $Ra = 1.6384 \times 10^8$. Practically all of the flux occurs on the sidewalls. Note that negative dips in the flux are evident inward of the sidewalls and result from hot (cold) fluid moving down (up), i.e., the “wrong” way. The detail on the right shows the structure of these negative dips as a function of Ra . The ordinate zero has been shifted by 15 for different values of Ra . Negative dips appear when $Ra > Ra_T$. Also, the negative dips betray a left-right asymmetry in the large-scale roll for $10^7 < Ra < 4 \times 10^7$ which we observe to persist for at least 240 “large-eddy” turnover times.

with a modulation of its amplitude on a time scale which is large compared to its period. Note the difference in the amplitude of the two signals. The period evident in the figure is simply the “large-eddy turnover time” and is identical (within “experimental” uncertainty) for both $\sigma=1$ and 7.

B. Heat transport

Returning to Fig. 5, which depicts the time-averaged vertical flux through the mid-height of the cell, we should note that the transport due to turbulent, small-scale fluctuations through the center of the cell is negligibly small; hence we conclude, immediately, that those theories emphasizing the turbulent transport of heat flux through the center of the cell fail to illuminate the relevant physics involved as the flow establishes the heat transport. How then is the heat flux carried through the cell in 2D hard turbulence?

First, heat flux diffuses into the cell through the bottom of the sheared, hot thermal boundary layer. This flux later emerges in the form of thermal plumes developing out of the top of the hot boundary layer. These

plumes are swept horizontally by the fluctuating “wind” and several coalesce to form a large plume near the downstream sidewall. Overcome by buoyancy, this large plume rises along the sidewall and in so doing carries heat flux away from the hot boundary layer. (Incidentally, the highest velocities obtained in the cell occur along the sidewalls and are due to these large buoyant plumes; hence plumes drive the large-scale circulation; see Fig. 7.) Eventually, the rising plume impacts the upper boundary layer in the corner where the sidewall meets the upper surface of the cell. In this corner, the plume is redirected horizontally; subsequently, it becomes a dominant part of the “wind” which sweeps along the upper boundary layer, exchanging heat flux directly with the sheared, cold boundary layer. Once inside the cold thermal boundary layer, heat flux diffuses out through the top of the cell. Notice that this scenario does not involve the central region of the cell in any way and certainly the transport properties of the central turbulence play, at best, a minor role.

Many aspects of this scenario are evident in Fig. 5. The large positive peaks attached to the sidewalls in the figure result from the large buoyant plumes ejected from the boundary layers. Because the large-scale flow for these runs happens to be clockwise, the peak on the left sidewall results from rising hot plumes while that on the right results from sinking cold plumes. The smaller negative dips toward the cell’s center result from plumes which have swept past the opposite boundary layer from which they have emerged and live sufficiently long to continue traveling with the large-scale flow, eventually moving in the “wrong” direction [i.e., with hot (cold) fluid moving downward (upward) near the right (left) sidewall]. In effect, these long-lived plumes are dragged around the cell by younger, more intense plumes.

It is interesting that the appearance of the hard-turbulent state for $\sigma=7$ coincides with the development of these plumes with sufficiently long lifetimes to move in the “wrong” direction. Note that the total negative heat flux occurring at $Ra = 1.024 \times 10^7$ is nearly zero; this value of Ra corresponds to the transitional Rayleigh number $Ra_T \approx 10^7$, at which hard turbulence appears.

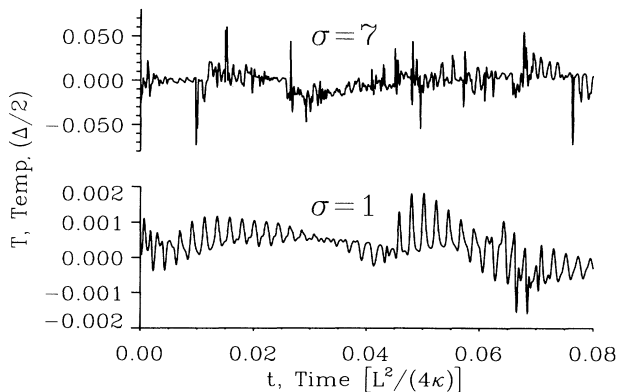


FIG. 6. A comparison of the time evolution of the temperature T for $\sigma=1$ and 7 near the middle of the cell ($x=0.125$, $z=0.0$). $Ra = 1.6384 \times 10^8$. The runs span roughly 40 turnover times.

No negative dips in the vertical heat flux occur for $Ra < Ra_T$. Tempting though it may be to assert that these negative dips are the hallmark of the hard-turbulent state, the steady solutions with $\sigma = 1$ (for which no simple dependence of Nu on Ra is evident) also exhibit negative dips and for Ra as low as 3.2×10^5 . Therefore negative dips in the vertical flux may exist independently of the hard-turbulent state.

Nevertheless, we do observe negative dips in the vertical flux and therefore we can make use of them to better understand the heat transport in hard turbulence. For example, because the negative dips in Fig. 5 are substantially smaller than the positive peaks adjacent to the

walls, we infer that a large fraction of the heat flux carried by a plume is deposited directly into the boundary layer as the plume passes by. In fact, this heat exchange between passing plumes and the boundary layer is

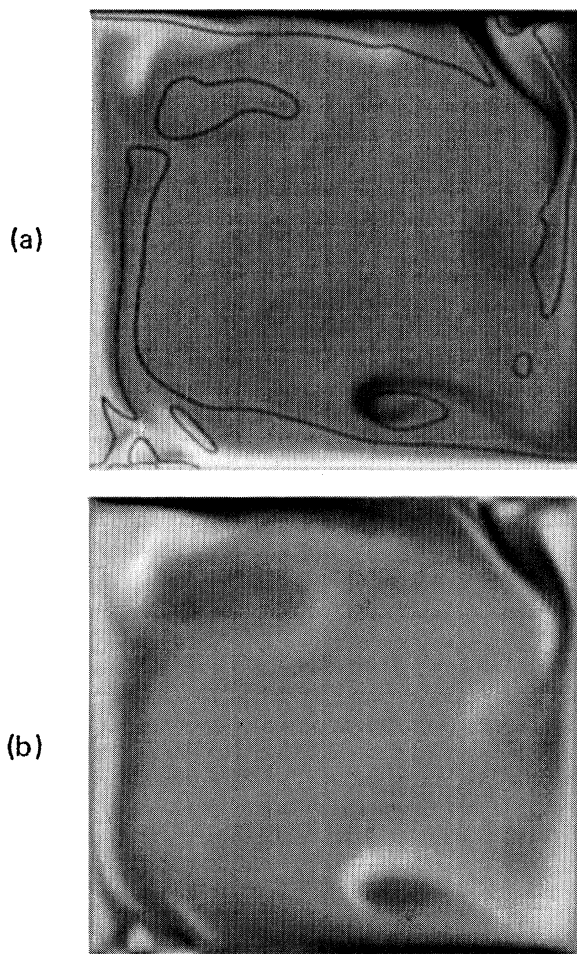


FIG. 7. The temperature (a) and the vorticity (b) for $Ra = 8.192 \times 10^7$ and $\sigma = 7$. Clockwise vorticity is shown as white. The contour for zero vorticity is superposed on the image of the temperature. The images demonstrate that newly formed plumes drive the large-scale circulation. The intense cold plume just emitted from the top boundary coincides with zero vorticity. Also, the sign of the vorticity indicates that the plume is forcing the fluid around it, rather than simply being dragged by the large-scale flow.

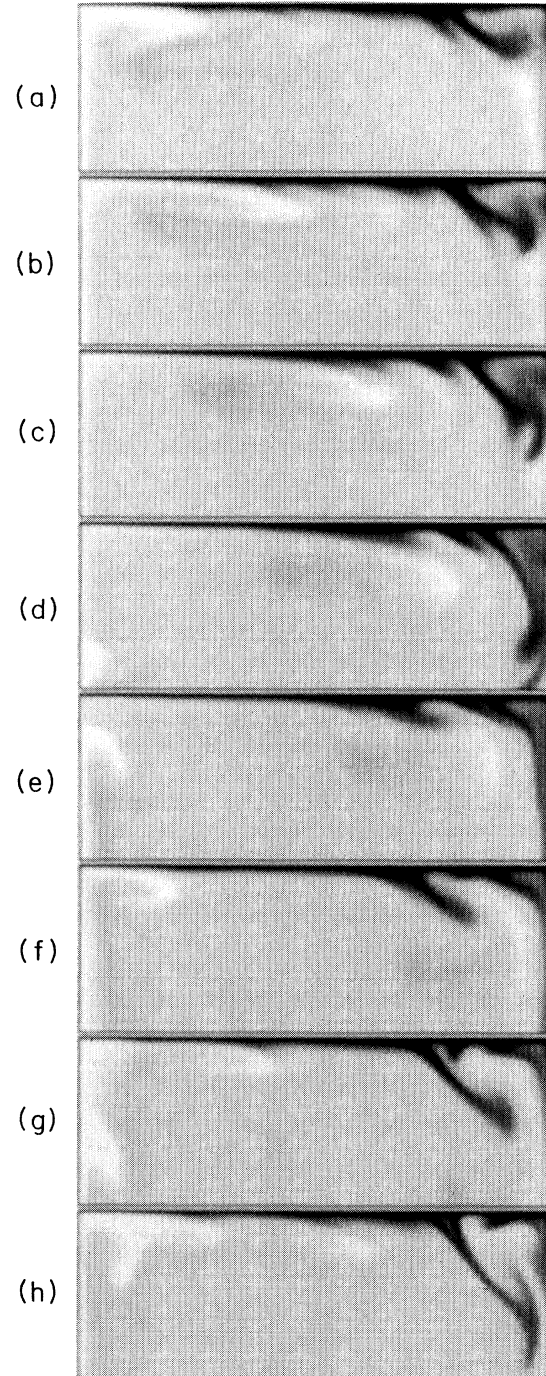


FIG. 8. Heat exchange between large hot plumes and the cold thermal boundary layer for $Ra = 8.192 \times 10^7$ and $\sigma = 7$. Each image shows the temperature field for the top 38% of the cell. (a)–(e) depict a hot plume as it sweeps across and exchanges heat with the cold boundary layer. (f)–(h) illustrate the coalescence of several cold plumes near the right corner.

sufficiently great that it can actually be seen by visualizing the temperature field.

The sequence of images depicted in Fig. 8 graphically illustrates the heat exchange between plumes and the thermal boundary layer. The first image [Fig. 8(a)] shows a hot plume as it impacts the top boundary layer. Images 8(b)–8(e) follow this plume as it skirts outside the cold boundary layer. The heat exchange between the plume and the boundary layer is evident in the noticeable decrease in the plume's thermal energy density (proportional to the temperature or shade of gray) as the plume travels. The remainder of the sequence [8(f)–8(h)] illustrates the coalescence of several cold plumes near the right-hand corner as they form a large plume which, in turn, sinks downward and impacts the hot boundary layer.

In order to quantify the importance of the exchange between the boundary layer and passing plumes to the overall heat transport in hard turbulence, we now consider the flux through the top and bottom of the cell in greater detail. To begin, Fig. 9 presents the horizontal dependence of the time-averaged heat flux through the top and bottom surfaces for several values of Ra in hard turbulence. First, note the near-perfect symmetry of the near-wall region of the hot and cold thermal boundary layers: Profiles for the heat flux through both boundaries are included in Fig. 9 and these profiles are nearly identical. Evident in the figure are three distinct regions along the top and bottom boundaries: (1) At the upstream corner ($-1.0 < x < -0.7$), heat transport is enhanced by the impact of incoming thermal plumes perpendicular to the boundary. (2) Immediately downstream of the corner ($-0.7 < x < 0.4$), redirected plumes travel horizontally and exchange heat with the boundary layer. The steady

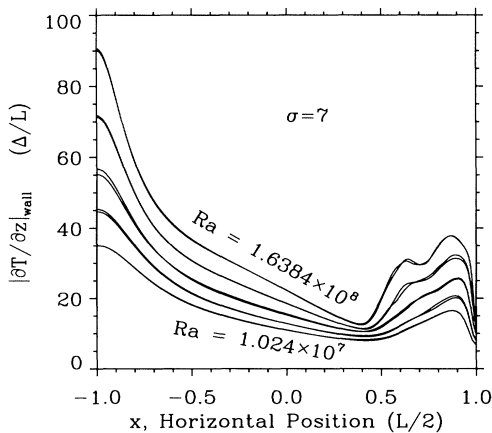


FIG. 9. Temperature gradient at the top and bottom boundaries in hard turbulence. The enhancement at the upstream corner of the cell ($-1 < x < -0.7$) is the result of intense incoming thermal plumes which impact the boundary layer. The steady decrease in the region $-0.7 < x < 0.4$ occurs as plumes sweep across the boundary layer, exchanging heat directly with the boundary layer. The enhancement near the downstream corner $\sim(0.4 < x < 1)$ results from the ejection of newly formed plumes from the boundary layer.

decrease in the heat transport in the streamwise direction results from spanwise spreading of the redirected plumes as well as the reduction in the plumes' thermal energy density resulting from heat exchange with the boundary. (3) Finally, near the downstream corner ($0.4 < x < 1.0$), heat transport is enhanced primarily by the ejection of large thermal plumes from the boundary. The relative importance of each of these regions to the global heat transport may be discerned by examining the fraction of the total heat flux through the entire boundary which passes through each of these regions. Figure 10 presents these fraction versus Ra .

For high Ra , the fraction of the heat transport through the upstream-corner region decreases markedly as Ra is increased above Ra_T : Though $\partial T/\partial z$ is maximal in this region, the peak in $\partial T/\partial z$ becomes sufficiently narrow as Ra is increased to make the net contribution to the global heat transport small. On the other hand, the middle region of the boundary, above which plumes travel horizontally, is responsible for a large fraction of the total heat flux as Ra is increased above Ra_T . The dominance of this middle region favors the theory of Shraiman and Siggia, which assumes that heat flux enters and exits the cell through strongly sheared thermal boundary layers. The compensation of the decreased transport through the upstream region [region (1)] by the increase through region (2) is in large part due to the definition of the midpoint separating these two regions; this point, chosen to locate the position at which the fluid velocity becomes "self-preserving," moves towards the upstream corner as

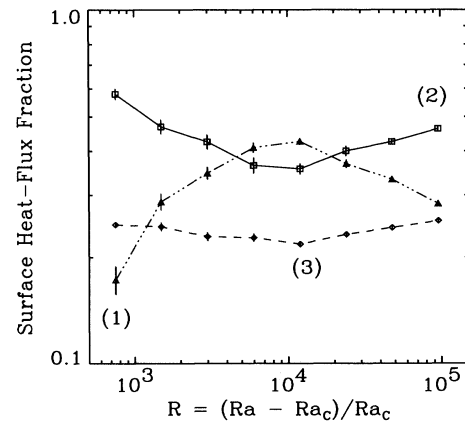


FIG. 10. Fraction of the heat flux through (1) the plume impacting, (2) the plume sweeping, and (3) the plume ejection regions of the top and bottom boundaries versus Ra for $\sigma = 7$. (Fig. 9 depicts these three regions.) Region (2) is defined as spanning the position near the upstream corner at which the horizontal velocity becomes self-preserving (see Fig. 15) to the point of separation where the heat flux is minimal; regions (1) and (3) take up the remaining portions of the boundary. The transition to hard turbulence is evident in the figure, reporting a change in the structure of the boundary layers at $Ra \approx Ra_T$. For $Ra > Ra_T$, region (2) dominates the total heat flux through the boundary.

Ra is increased, signaling the overtaking of region (1) by region (2). (More will be said about self-preserving wall layers below.) Near the downstream corner, where plume ejection takes place, the contribution to the total heat flux increases slightly with Ra and is $\sim 20\%$. Of course, if hard turbulence is the asymptotic state for high-Ra, Boussinesq convection, these fractions will not increase or decrease indefinitely and will obtain limiting values as $Ra \rightarrow \infty$ and the *entire* extent of the boundary layer develops a scaling behavior with Ra. Obviously, our simulations cannot address the asymptotic nature of turbulent convection for $Ra \rightarrow \infty$ [27]. Nevertheless, it is apparent from Fig. 10 that the heat exchange with passing plumes in region (2) of the boundary dominates the global heat transport for high Ra; therefore we now consider the central region in greater detail.

In order to quantify the efficiency with which passing plumes exchange heat with the central portion of the boundary layers, we estimate the average fraction of a plume's thermal energy, which is deposited directly into the boundary layer as it passes by, by considering the time-averaged profile for the horizontal component of the heat flux along the boundary. Figure 11 presents the horizontal flux adjacent to the top boundary for $Ra = 1.6384 \times 10^8$ and $\sigma = 7$. In the figure, incoming hot plumes travel from the leftmost corner of the cell to the right. (The spatial geometry is identical to that of the images in Fig. 8.) The flux is negative nearest the top boundary because the temperature of the fluid is less than the mean temperature in this region and the fluid is moving in the positive x direction. Just outside the thermal boundary layer, the flux is positive because the fluid in this region is comprised primarily of hot plumes also

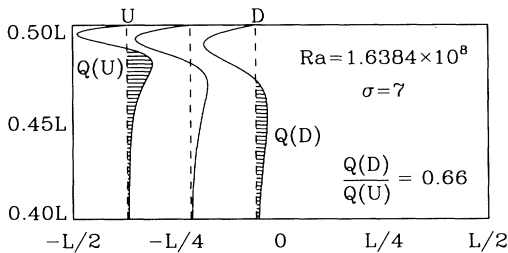


FIG. 11. Horizontal heat-flux profile near the top boundary: Heat exchange between the boundary layer and passing plumes. Three profiles of $\langle Tu - \partial T / \partial x \rangle_t$ are presented in the region along the upper boundary layer for which the flow is self-preserving (see Fig. 15). The shaded regions $Q(U)$ and $Q(D)$ represent the average heat flux carried by hot plumes as they pass the upstream $x = U = -0.73$, and the downstream positions, $x = D = -0.12$. The ratio $Q(U)/Q(D)$ is related to the amount of flux deposited by hot plumes into the cold boundary layer as the plumes sweep by between $x = U$ and D . The integral of the horizontal heat flux at the upstream and downstream positions is computed from the mid-height of the box, $z = 0$, to the position near the thermal boundary layer at which the mean horizontal heat flux is zero. Also, the downstream flux $Q(D)$ is corrected by subtracting the small amount of flux which enters across the $z = 0$ line between $x = U$ and D .

moving to the right. The shaded areas $Q(U)$ and $Q(D)$ represent the average rate at which heat is carried by plumes past the horizontal position at which the profile is plotted. The average proportion f_T of the heat carried by plumes which is transferred directly to the cold thermal boundary layer between U and D is related to the ratio of the shaded areas $Q(D)/Q(U)$:

$$f_T = 1 - \frac{Q(D)}{Q(U)}. \quad (4)$$

For $Ra = 1.6384 \times 10^7$ and $\sigma = 7$ and the distance between the upstream (U) and downstream (D) positions spanning just 31% of the box width L , we find $f_T = 0.34$. Therefore, on the average, a good deal of the plume's thermal energy is transferred directly to the boundary layer as the plume passes by.

Estimates of f_T for $(U - D)/L = 0.20$ are plotted versus Ra in Fig. 12 for both $\sigma = 1$ and 7. The fact that f_T can be measured for the time-independent solutions with $\sigma = 1$ simply indicates that the "passing plumes" in this case should be considered as long extensions of the opposite thermal boundary layer (i.e., the "plumes" in this case are not dynamic objects but rather steady features of the large-scale flow). The fraction f_T for $\sigma = 1$ is greater than that for $\sigma = 7$ because the viscous boundary layer is thinner relative to the thermal boundary layer for $\sigma = 1$. Hence, incoming "plumes" penetrate more deeply into the thermal boundary layer and, as a result, exchange heat more efficiently with $\sigma = 1$.

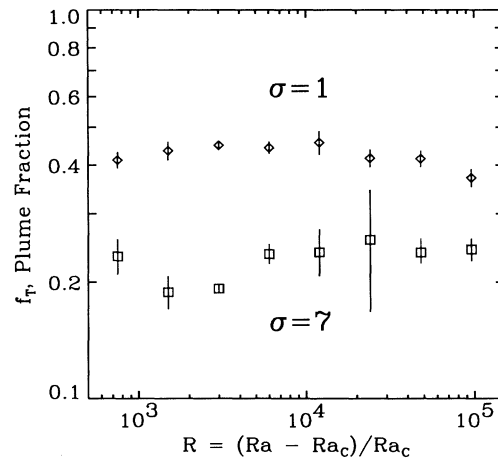


FIG. 12. f_T vs R for $\sigma = 1$ and 7. f_T is the fraction of a plume's heat flux which is deposited directly into the opposite boundary layer. The upstream, U , and downstream, D , positions span 20% of the box width. U is selected to coincide with the point separating regions (1) and (2), the position at which the flow becomes self-preserving for $\sigma = 7$; see Fig. 15. The runs with $\sigma = 1$ do not develop self-preserving wall layers; therefore selection of U for these runs is ambiguous and we use the same position chosen for $\sigma = 7$ for lack of a better choice. The error bars result from the uncertainty in locating U for $\sigma = 7$ as well as the disparity between the results for the top and bottom boundaries.

C. Boundary-layer structure

A theory of the efficiency with which plumes exchange heat flux with the thermal boundary layer and the rate at which heat flux enters and exits the cell requires a picture of the detailed structure of the viscous and thermal boundary layers. Figure 13 presents part of such a picture: The figure shows the terms in the time-averaged horizontal momentum and heat equations in the central region of the boundary layer for $Ra=1.6384 \times 10^8$ and $\sigma=7$. For reference, peaks in the velocity and tempera-

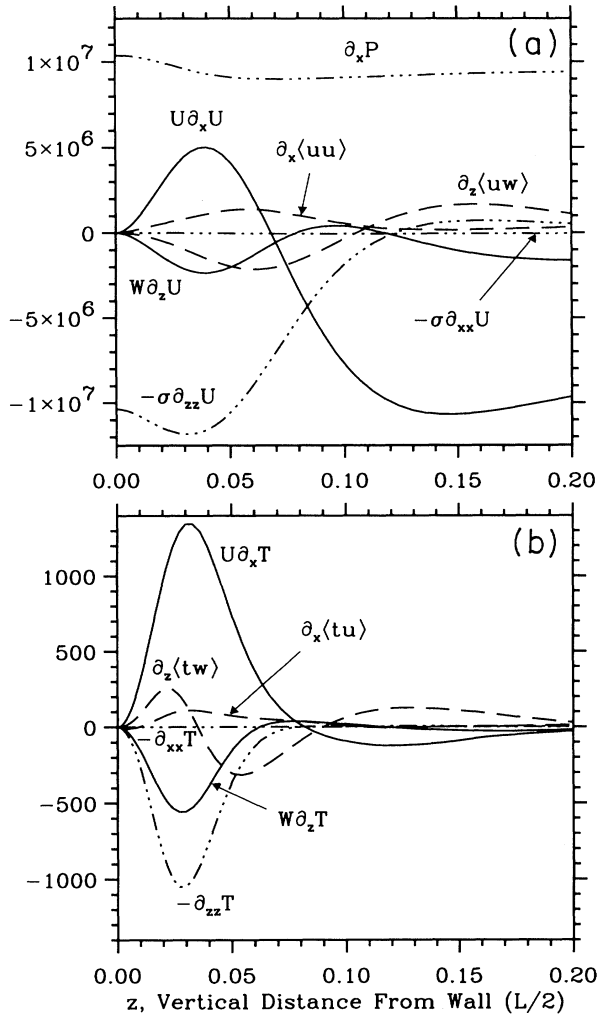


FIG. 13. Horizontal-momentum- [(a), Eq. (1)] and heat-equation profiles [(b), Eq. (2)] near the bottom boundary for $Ra=1.6384 \times 10^8$ and $\sigma=7$. The profiles are plotted for $x=-0.41$, at the middle of the self-preserving region of the boundary layer (see Fig. 15). Mean, i.e., time-averaged, quantities are denoted with upper-case symbols while fluctuating quantities carry lower-case symbols. Angular brackets denote time-averaging. Solid lines are used for the mean advection terms while dashed lines denote advection by the fluctuations. The dot-dashed lines represent the diffusive terms.

ture profiles (i.e., roughly the boundary-layer thicknesses, δ and λ defined below) occur at distances from the wall of $0.079(L/2)$ and $0.044(L/2)$, respectively. It is evident that the standard boundary-layer assumption ($\partial_z \gg \partial_x$) is appropriate while the other assumption typically made for boundary-layer flow ($\partial_x P$ not a function of z) appears marginal.

Evident in the figure is that neither of the assumptions made by Shraiman and Siggia [13] [(1) pipe-flow profiles and (2) thermal layer much less than laminar sublayer] are clearly applicable: A pipe-flow profile requires $W=\partial_x U=\partial_x \langle uu \rangle=0$ (using the notation adopted in Fig. 13), while a thermal layer nestled completely within the laminar sublayer results in $\partial_x \langle tu \rangle=\partial_z \langle tw \rangle=0$; also, assumption (2), concerning the relative heights of the thermal and viscous boundary layers, requires the variations in the heat-equation profiles to be confined much closer to the surface than the variations in the momentum-equation profiles. The agreement of Fig. 13 with these assumptions is not particularly compelling. Nevertheless, the scaling relationships ($Nu \propto Ra^{2/7}$, $\partial u/\partial z \propto Ra^{6/7}$) derived from the assumptions in [13] are obtained; see Fig. 14. One must conclude therefore that the scaling relationships result more generally than is apparent in [13].

Though we do not present here a more general version of the boundary-layer analysis in [13], we do present some features of the viscous and thermal layers which we hope will prove useful in constructing a more general theory. The boundary layers we observe for 2D hard turbulence have so-called self-preserving profiles:

$$u(x,z)=u_0(x)\xi(\eta_u), \quad \eta_u=z/\delta(x), \quad (5)$$

$$T(x,z)=1-T_0(x)\zeta(\eta_T), \quad \eta_T=z/\lambda(x). \quad (6)$$

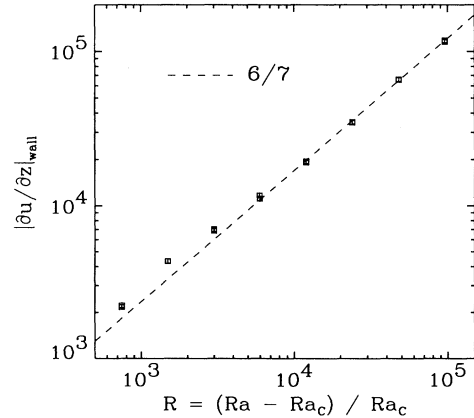


FIG. 14. Velocity gradient at the top and bottom boundaries for $\sigma=7$. The gradient is obtained at the middle of the self-preserving region of the boundary layer (see Fig. 15). These results for hard turbulence ($Ra > Ra_T$) are consistent with the $\frac{6}{7}$ law predicted by Shraiman and Siggia [13]. The uncertainty in the data points is roughly the size of the symbols and results from the uncertainty in locating the middle of the walljet as well as the disparity between the results for the top and bottom boundaries.

For the velocity field, this type of profile is called a “walljet” or “equilibrium layer” [28,29]. The length scale $\delta(x)$ defines the vertical distance from the boundary at which the maximum velocity $u_0(x)$ occurs. Similarly, $\lambda(x)$ defines a characteristic thickness of the thermal layer and $T_0(x)$ is the magnitude of the temperature difference (from the wall) at $z=\lambda(x)$. The functions $\xi(z/\delta)$ and $\zeta(z/\lambda)$ describe the velocity and temperature profiles in the z direction. As the flow develops in the x direction, the profiles are simply rescaled by $\lambda(x)$, $\delta(x)$, $T_0(x)$, and $u_0(x)$; see Figs. 15(a) and 15(b). (Also, see Fig. 16 for the x dependence of λ , δ , T_0 , and u_0 .) Both the temperature and velocity fields exhibit self-preserving profiles only from $x \approx -0.7$ to $x \approx 0.0$ [i.e., not throughout all of region (2), the central portion of the boundary layer from $x \approx -0.7$ to $x \approx 0.4$]. Downstream of $x \approx 0.0$, the velocity profile becomes non-self-preserving because the flow separates ($\partial u / \partial z = 0$) near $x \approx 0.4$. Flow separation is unavoidable here because of the existence of the downstream sidewall. Presumably the temperature profile also develops in a non-self-preserving way downstream of $x \approx 0.0$ because of the coupling between the temperature and velocity fields.

Figures 15(c) and 15(d) illustrate the algebraic scaling with Ra of the boundary layers in 2D hard turbulence. Profiles at different Ra are included in Figs. 15(c) and 15(d) and they are identical in the range $0 < \eta_u, \eta_T < 1$; therefore a universal structure (i.e., ξ and ζ) for the near-

wall region exists for hard turbulence and this structure is simply rescaled (by λ , δ , T_0 and u_0) as Ra is increased beyond Ra_T . This simple scaling of the temperature and velocity profiles results in the power laws $\partial u / \partial z \propto Ra^{6/7}$ and $Nu \propto Ra^{2/7}$ when $Ra > Ra_T$. In contrast, for $Ra < Ra_T$, the velocity profile, though self-preserving, deviates from the universal shape ξ and as a result $\partial u / \partial z$ does not exhibit the power-law dependence on Ra .

To demonstrate the deviation of ξ for $Ra < Ra_T$, Fig. 17 shows the fractional deviation of the profiles at different values of Ra from the profile obtained with $Ra = 1.6384 \times 10^8$. We define the fractional deviation for the velocity profile, $\Delta u / u$, as follows:

$$\left[\frac{\Delta u}{u} \right]^2 = \frac{1}{N} \int_0^1 [\xi(\eta_*, Ra) - \xi(\eta_*, Ra_*)]^2 d\eta_*,$$

where

$$N = \int_0^1 [\xi(\eta_*, Ra_*)]^2 d\eta_*$$

and

$$\eta_* = \frac{z}{\delta(x_*)}.$$

Here, $Ra_* = 1.6384 \times 10^8$ and x_* is the location of the middle of the walljet. $\Delta T / T$ is defined in a similar manner using ζ and λ . For $Ra > Ra_T$, the percent devia-

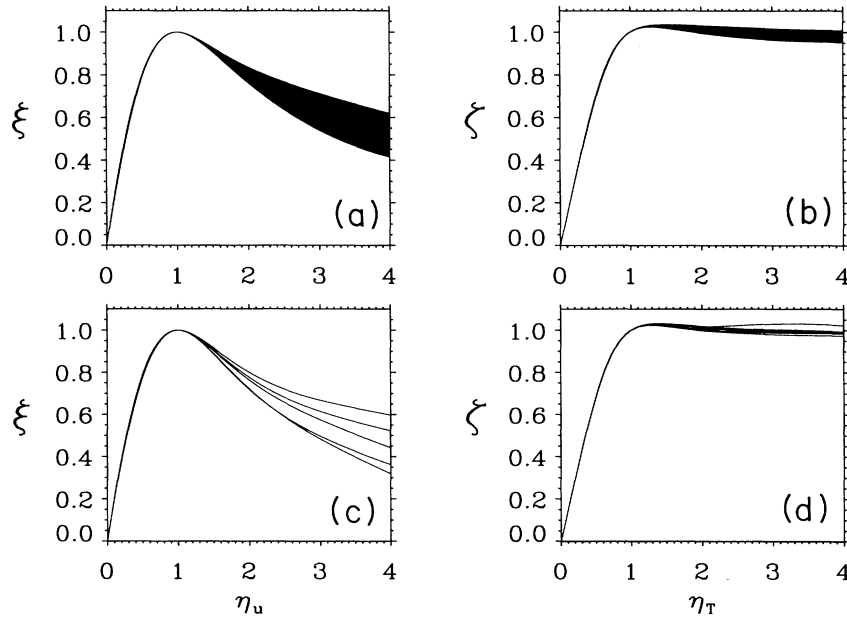


FIG. 15. Self-preserving wall layers in hard turbulence. (a) and (b) show the velocity and temperature profiles for $Ra = 1.6384 \times 10^8$ and $\sigma = 7$ throughout the walljet ($-0.7 < x < 0.0$). Whereas the profiles are independent of x , i.e., are self-preserving, for $0 < \eta_u, \eta_T < 1$, the profiles exhibit x dependence for $\eta_u, \eta_T > 1$ where they must merge with the large-scale roll in the center of the cell. This x dependence is evident in the spread in the profiles for $\eta_u, \eta_T > 1$. (c) and (d) depict the universality of the velocity and temperature profiles in hard turbulence. (c) shows the velocity profiles for Ra of 1.024×10^7 through 1.6384×10^8 and $\sigma = 7$. The self-preserving region $\eta_u < 1$ is identical for all of these Ra and hence ξ exhibits simple scaling behavior with Ra . Similar scaling behavior is exhibited in (d) for the temperature profile ζ . The temperature profiles differ from the velocity profiles in that scaling is exhibited for the temperature profiles for Ra both above and below Ra_T . All of the runs ($1.28 \times 10^6 < Ra < 1.6384 \times 10^8$) are included in (d) and all of the profiles are identical.

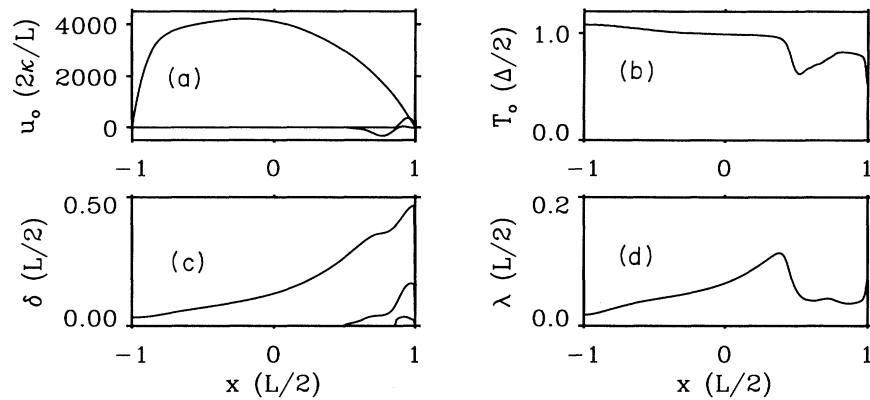


FIG. 16. Length, velocity, and temperature scales for the boundary layers in hard turbulence with $Ra=1.6384 \times 10^8$ and $\sigma=7$. These scales (in the range $-0.7 < x < 0.0$) are used to rescale the profiles ξ and ζ so that they may be overlaid in Figs. 15(a) and 15(b). The upstream corner of the flow is at $x = -1$. (a) shows the peak horizontal velocity u_0 vs x [the velocity at $\eta_u=1$ in Fig. 15(a)]. Directly below u_0 , the velocity length scale δ (the height at which $\partial u/\partial z=0$) is plotted in (c). Note that the maximum horizontal velocity increases from the upstream corner as incoming plumes are redirected and travel along the boundary. Downstream of $x=0$, the maximum velocity decreases as a result of spreading typical of walljets. (c) depicts this jet spreading in the downstream direction. The additional curves in (a) and (c) for $x > 0.4$ result from flow separation. (b) and (d) depict the temperature scale and the thermal length scale, respectively. From (b) we see that the temperature scale of the boundary layer is slightly greater than 1 at the upstream corner of the cell. This results because the incoming plumes which strike the boundary layer carry fluid directly from the opposite boundary. T_0 decreases in the downstream direction because of the heat exchange between the incoming plumes and the boundary layer. (This exchange acts to decrease the temperature contrast between incoming plumes and the boundary layer.) (c) shows the spreading of the thermal boundary layer in the downstream direction.

tion in u , $\Delta u/u$, is $\lesssim 1.5\%$, while, in contrast, for $Ra < Ra_T$, $\Delta u/u$ is systematic and increases with decreasing Ra . $\Delta T/T$, on the other hand, exhibits no systematic trend for $Ra < Ra_T$. Hence a fundamental change in the viscous boundary layer occurs at $Ra \approx Ra_T$, while no such change takes place in the thermal boundary layer: For $Ra < Ra_T$, a self-preserving wall layer exists, but its velocity profile depends on Ra ; for $Ra > Ra_T$, the velocity profile is independent of Ra and simple scaling behavior is exhibited. For the temperature, a unique (i.e., independent of Ra), self-preserving profile ζ is obtained for Ra both above and below Ra_T . Therefore the change in the scaling of Nu with Ra results from the Ra dependence of the temperature and thermal length scales, T_0 and λ , rather than from a change in the shape of the temperature profile. Presumably, this change in the Ra dependence of T_0 and λ is related to the change in the velocity profile ξ .

An important matter which must be addressed when constructing a theory of the heat transport through the boundary layers in hard turbulence is whether the structure of the boundary layer is truly determined by two length scales (e.g., δ and λ) or simply by one (i.e., $\delta=C\lambda$, $C=\text{const}$). In order to address this issue, we plot the ratio δ/λ vs x for $Ra=1.6384 \times 10^8$; see Fig. 18(a). It is evident from the figure that δ/λ is only poorly approximated by a constant throughout the central portion of the boundary [region (2)]; the insert shows that δ/λ varies by $\sim 14\%$ in this region. This indicates that at least two length scales are indeed required to describe the structure of the boundary layer in hard turbulence. Fig-

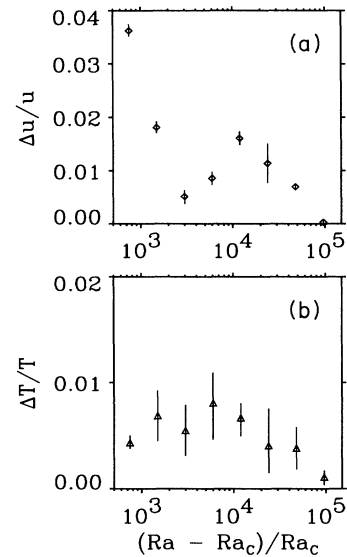


FIG. 17. Fractional deviation of walljet profiles versus Ra for $\sigma=7$. (a) shows the deviation in the velocity profile $\Delta u/u$ while (b) shows the deviation in the temperature profile $\Delta T/T$. The velocity profiles in hard turbulence are all similar and exhibit a deviation from each other of $\sim 1.5\%$ or less. For $Ra < Ra_T$, a systematic increase in $\Delta u/u$ with decreasing Ra is evident. In contrast, $\Delta T/T < 1\%$ even for $Ra < Ra_T$. The error bars are estimated from the disparity in the results from the top and bottom boundaries. Fractional deviations are reported with respect to the profiles with $Ra=1.6384 \times 10^8$.

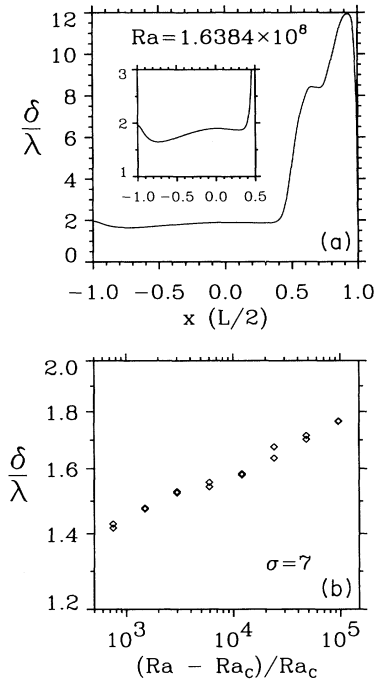


FIG. 18. Ratio of the velocity and temperature length scales (δ and λ) in hard turbulence. (a) shows δ/λ vs x for $Ra = 1.6384 \times 10^8$ and $\sigma = 7$. The ratio exhibits noteworthy x dependence ($\sim 14\%$) in the region in which the flow is self-preserving ($-0.7 < x < 0$); see inset. (b) shows δ/λ at the middle of the walljet versus Ra . Note that λ shrinks faster than δ as Ra is increased.

ure 18(b) further supports this observation by presenting δ/λ at the middle of the walljet as a function of Ra . Note that the ratio δ/λ increases slightly with Ra .

Several observations can be made concerning Fig. 18. First, it is apparent that the assumption $\delta/\lambda \gg 1$ made in [13] is not valid for our solutions (this conclusion has already been drawn based on Fig. 13). Hence $\delta/\lambda \gg 1$ is certainly not a prerequisite for obtaining the heat-transport scaling $Nu \propto Ra^{2/7}$. (We should note, however, that we have only observed hard turbulence to occur when $\delta/\lambda \gtrsim 1.55$; hence $\delta/\lambda \gtrsim 1.55$ may be a requirement to obtain hard turbulence.) Second, the conclusion drawn in [13] that hard turbulence must break down as $Ra \rightarrow \infty$ is not supported by our results. This conclusion is drawn in [13] based on the proposal that λ will eventually become larger than δ at sufficiently high Ra . The proposal follows directly from the assumptions in [13] which we have already demonstrated are not valid for our 2D solutions. Furthermore, our solutions exhibit a thermal boundary layer which shrinks more rapidly than the viscous boundary layer as Ra is increased; see Fig. 18(b). Therefore, for 2D hard turbulence to break down as $Ra \rightarrow \infty$, some mechanism other than $\lambda > \delta$ is required.

V. CONCLUSION

The 2D simulations represented here illustrate the important role played by the large-scale circulation in

hard-turbulent convection. The organized large-scale flow provides plumes an efficient means to transport heat directly between opposing boundaries. The large-scale flow also produces a stabilizing shear on the thermal boundary layers. For $\sigma = 7$, this boundary-layer shear flow exhibits simple scaling behavior, while the large-scale structure of the center of the cell does not; see Fig. 5. This should be compared with the situation with $\sigma = 1$ for which the boundary layers do not exhibit simple scaling behavior. Considering that the $\sigma = 7$ solutions exhibit hard-turbulent behavior while the $\sigma = 1$ solutions do not, the numerical solutions strongly imply the importance of the structure of the boundary layers in determining the heat transport.

Of the attempts to derive the heat-transport scaling relationship $Nu \propto Ra^{2/7}$ [4,13–15] the general approach by Shraiman and Siggia appears most appropriate. In contrast, the other theories which attempt to explain the Nu - Ra scaling in hard turbulence rely (either in part or in full) on the transport characteristics of the small-scale fluctuations in the center of the cell. For our 2D simulations, however, the dominant mechanism for heat transport is via the direct heat exchange between a thermal boundary layer and coherent plumes emitted from the opposite boundary. Because the plumes travel with the large-scale circulation directly from one boundary layer to the other, heat-transfer mechanisms involving the small-scale fluctuations in the cell's center play only a secondary role.

Though the *general* approach by Shraiman and Siggia captures the flavor of hard turbulence as it appears in our 2D simulations, specific assumptions made by Shraiman and Siggia [(1) and (2) mentioned above] are not borne out by our solutions. Nevertheless, the scaling relationships derived by Shraiman and Siggia ($Nu \propto Ra^{2/7}$ and $\partial u/\partial z \propto Ra^{6/7}$) are observed by us. We conclude therefore that the assumptions in [13] are unnecessarily restrictive and that the above scaling relationships are more general than is evident from [13]. A consequence of the fact that the flow need not satisfy the assumptions in [13] in order to exhibit the scaling relationships associated with hard turbulence is the possibility of hard turbulence existing in the asymptotic limit as $Ra \rightarrow \infty$; our 2D solutions (for Ra up to 1.6×10^8) support this possibility.

ACKNOWLEDGMENTS

The numerical algorithm used to obtain the results presented here was developed by Fausto Cattaneo and Ed E. DeLuca. In addition, this work has benefited from illuminating discussions with L. Kadanoff, M. Leibig, A. Libchaber, and R. Rosner. The computations were performed using the CRAY/Y-MP8/864 supercomputer at the National Center for Atmospheric Research in Boulder, Colorado. This work was supported by the NASA Space Physics Theory Program at the University of Chicago.

APPENDIX: LARGE-SCALE ROLL

As has been discussed above, a dominant feature of both the 3D and 2D hard-turbulent flows in the unit-

aspect-ratio configurations is a coherent, large-scale organization of the flow into a single convective roll [1,3,6,7,12]. Flows with aspect ratios $\gg 1$ are expected to develop multiple convection “cells” positioned side-by-side, as is the case for low-Ra convection [17]. Of course, for high-Ra convection, individual rolls in large-aspect-ratio containers will have only finite lifetimes and will be replaced by newly formed rolls due to the inherent instability of highly driven flows. Nevertheless, we expect the general characteristics of our unit-aspect-ratio solutions to shed some light on the properties of hard turbulence in large-aspect-ratio containers.

Issues with which we will be concerned in this appendix include (1) the turnover time of the roll, (2) a nearly solid-body rotation exhibited in the central portion of the roll, and (3) the nature of the transition in the structure of the large-scale roll which occurs at $Ra \approx 4 \times 10^7$.

1. Turnover time and ω_p

One of the features characteristic of hard turbulence is a prominent peak in the temporal power spectrum of a time trace collected at a fixed position in the cell; see Fig. 19. The time trace may be the result of any field (e.g., T , P , or $|\mathbf{v}|$) and the frequency associated with the peak is called the coherence frequency ω_p . It has been suggested that the frequency ω_p is merely an artifact of the large-scale roll in hard turbulence; in particular, $2\pi/\omega_p$ has been interpreted as the turnover time of the large-scale roll [1]. We will demonstrate explicitly that this is indeed the case.

To begin, an indication of the relationship of ω_p to the large-scale roll is evident in Fig. 20, which presents the signal-to-noise ratio of ω_p as a function of position inside the cell for $Ra = 8.192 \times 10^7$. The prominent “ring” centered at the middle of the roll demarcates the region in which fragments of thermal plumes circulate with the large-scale rotation. In this central region, plume fragments remain coherent for as long as five rotations of the large-scale circulation; hence the signal has a strong periodic component at ω_p . The absence of a strong ω_p peak in the exact center of the roll results because it is extremely rare for plume fragments to enter this region.

The relationship between ω_p and the large-scale flow is made precise by considering the time τ required for individual fluid elements to travel along closed trajectories in the mean velocity field. Figure 21 depicts a few of the

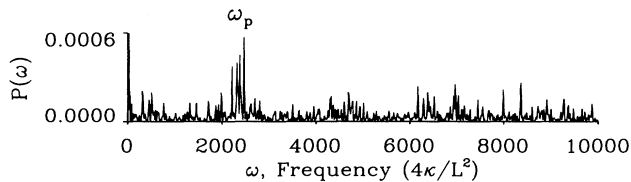


FIG. 19. Temporal power spectra for $Ra = 8.192 \times 10^7$ and $\sigma = 7$ for the temperature at $x = -0.4(L/2)$, $z = -0.7(L/2)$ (near the bottom boundary). the signal-to-noise ratio for ω_p is ~ 2 . The length of the time trace used to construct this power spectrum is $202(2\pi/\omega_p)$.

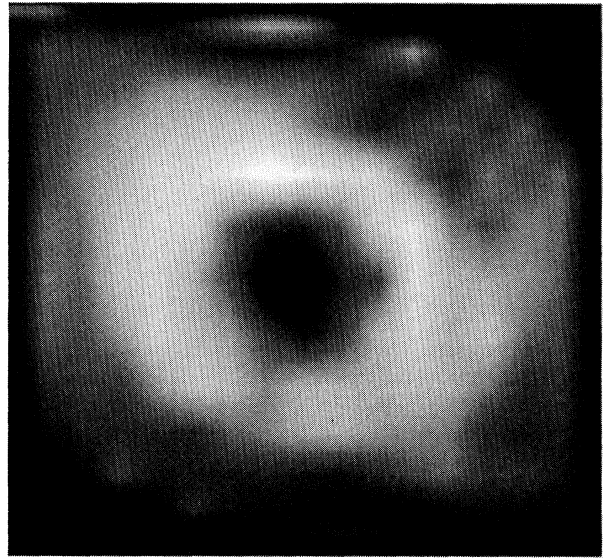


FIG 20. Signal-to-noise ratio of ω_p obtained with time traces of the temperature for $Ra = 8.192 \times 10^7$ and $\sigma = 7$. The prominent “ring” demarcates the path along which fluctuations are most pronounced. The figure is constructed using a coarse spatial subgrid (17×17 grid points) for 202 turnover times.

streamlines associated with the mean velocity field for $Ra = 8.192 \times 10^7$. The streamline depicted with the solid line has the period $\tau_0 = 2\pi/\bar{\omega}_p$, where $\bar{\omega}_p$ is the value of ω_p obtained from the spatially averaged spectrum. The streamlines located within this τ_0 streamline have periods which differ only slightly from τ_0 . Exactly how the period varies between individual streamlines is depicted in Fig. 22; this figure shows the radial dependence of the circulation frequency $\omega(r) = 2\pi/\tau(r)$, where r is the radial distance from the center of the cell. [The reader should note that $\omega(r)$ is obtained solely from the mean velocity field; the power spectrum is not utilized in obtaining $\omega(r)$.] Because the streamlines are not circular, $\omega(r)$ is

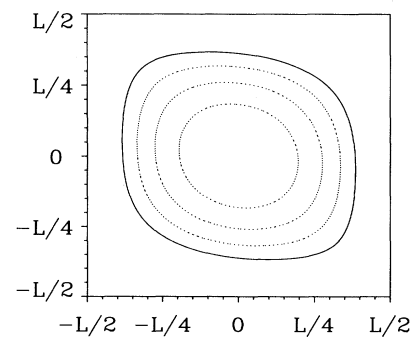


FIG. 21. Streamlines for the mean velocity field in hard turbulence ($Ra = 8.192 \times 10^7$ and $\sigma = 7$). The solid line shows the streamline with the frequency $\bar{\omega}_p$ obtained by spatially averaging the spectrum over the entire cell. The dotted lines show streamlines with frequencies slightly higher than $\bar{\omega}_p$.

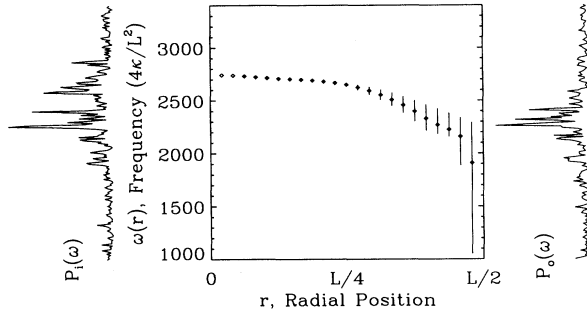


FIG. 22. Circulation frequency $\omega(r)$ versus radial position r for $\text{Ra} = 8.192 \times 10^7$ and $\sigma = 7$. The error bars depict the range in $\omega(r)$ for different streamlines crossing the circle with radius r . (Individual streamlines are not circular). The power spectra to the left and right of the plot are spatially averaged over the central 25% and the outer 75% of the cell, respectively. The core rotates nearly like a solid body and its frequency Ω_i is higher than the frequency near the cell boundaries, Ω_o ; the ω_p peak in the spectra reflects this higher rotation frequency Ω_i in the core.

not unique for a given r . In the figure, the range in $\omega(r)$ (represented by the error bars) demonstrates the range in circulation frequencies for the streamlines which cross the circle with radius r . Near the center of the cell, for which the streamlines are nearly circular, the range in $\omega(r)$ is small. Towards the edges of the cell ($r \rightarrow L/2$), $\omega(r)$ spans a large range resulting from the drastically different circulation times associated with those fluid elements passing near the free-slip sidewalls and for those moving within the viscous boundary layers on the top and bottom boundaries.

The validity of the suggestion that $2\pi/\omega_p$ is equivalent to the turnover time $2\pi/\omega(r)$ is demonstrated by the power spectra flanking the plot of Fig. 22. These two spectra are spatially averaged over two different regions within the cell. The spectrum on the right, $P_o(\omega)$, is the average spectrum for the outer 75% of the cell ($x, z > +0.5$ and $x, z < -0.5$). For this spectrum, the ω_p peak is characteristic of the low mean circulation frequency in the outer portions of the roll, Ω_o . To the left of the plot, the spectrum $P_i(\omega)$ is the result of a spatial average over the remaining inner 25% of the cell ($-0.5 \leq x, z \leq +0.5$). Notice that the ω_p peak in this spectrum has more power towards higher ω than $P_o(\omega)$. This high-frequency component encompasses the higher circulation frequency at the center of the cell, $\Omega_i = \omega(0)$. The reason $P_i(\omega)$ also reflects the outer circulation frequency Ω_o is because this frequency is communicated throughout the entire cell via the eruption of thermal plumes from the boundary layers. Hence the spatial dependence of $\omega(r)$ is reflected in the spatial dependence of ω_p and we can see explicitly that ω_p contains information about the mean turnover time. This identification of ω_p with the circulation frequency of the flow holds for all of the runs conducted and firmly establishes the interpretation of $2\pi/\omega_p$ as a circulation time in the cell.

2. Solid-body rotation

Aside from identifying $2\pi/\omega_p$ as the turnover time for the large-scale roll, more can be learned about the structure of 2D hard turbulence from Fig. 22. A noteworthy feature of the large-scale roll is that the core of the roll rotates nearly like a solid body. This can be discerned by the flatness of $\omega(r)$ near $r=0$ [i.e., $\partial\omega(r)/\partial r \approx 0$]; the fact that $\partial\omega(r)/\partial r$ is not identically zero betrays some shear in the large-scale rotation. Also, it should be noted that the core rotation frequency Ω_i is the highest circulation frequency obtained in the cell.

The fact that the central part of the roll rotates *nearly* like a solid body results because most of the forcing, which acts to “stir” the fluid in the cell, takes place near the boundaries. In fact, the plume fragments which maintain their coherence sufficiently long to venture into the central part of the roll exhibit only a small temperature difference from the mean temperature and are thus essentially passive. The extent to which solid-body rotation fails to describe the motion of the large-scale roll is indicated by the slight increase in the circulation frequency towards the center of the roll. This increase in the central rotation rate occurs because the large-scale stirring, which results from large thermal plumes circulating near the boundaries, is not confined completely to the boundary region itself; as the large, stirring thermal plumes circulate, they spread inward and, as a result, they enhance the forcing in the central region.

3. Transition in the large-scale roll

The secondary transition which occurs within the 2D hard-turbulent state is most pronounced in a plot of the Ra dependence of ω_p ; see Fig. 4. Both the core rotation frequency Ω_i (obtained from the central portion of the mean velocity field), and the outer-roll frequency Ω_o (obtained by averaging the spectrum over the outer 75% of the cell), are included in the figure. The scaling suggested by the experiment of Heslot, Castaing, and Libchaber [1] ($\omega_p \propto \text{Ra}^{1/2}$) has been divided out of both Ω_o and Ω_i by multiplying the frequencies by $R^{-1/2}$ before plotting them in Fig. 4.

Note that the numerical results exhibit a power-law dependence of Ω_o on R below $R \approx 24\,000$ ($\text{Ra} \approx 4 \times 10^7$) and that this power law is consistent with the exponent $\frac{1}{2}$; Ω_i exhibits a more complex Ra dependence for this range of Ra. The transition of the large-scale roll at $\text{Ra} \approx 4 \times 10^7$ is clearly evident in the figure through both Ω_i and Ω_o . Recall that this transition is associated with the symmetry of the large-scale roll; see Fig. 5. Furthermore, recall that no feature besides the coherence frequency ω_p has been observed to reflect this transition through its scaling with Ra. Many of the unaffected features include properties associated with the flow near the boundaries: Nu [11], $\partial u/\partial z$, as well as the sidewall temperature T_s and velocity V_s [12]; hence it is apparent that the exact structure of the flow in the central portion of the roll is unimportant in determining the characteristics of the flow near the boundaries. It is possible that

the flow in the central portion of the cell, comprising the large-scale roll, simply adjusts to the conditions imposed by the flow near the boundaries and that these conditions, combined with the geometrical constraint of two-

dimensionality, are incompatible with a self-similar structure, i.e., independent of Ra , for the large-scale roll with $10^7 < Ra < 4 \times 10^7$. The root of this transition therefore is probably the result of confining the flow in 2D.

-
- [1] F. Hetsch, B. Castaing, and A. Libchaber, *Phys. Rev. A* **36**, 5870 (1987).
- [2] A Rayleigh-Bénard cell is a container filled with fluid and heated from below. The Rayleigh number is the nondimensional temperature difference driving the heat transport and is given by $Ra = g\alpha\Delta L^3/(\nu\kappa)$, where g is the local acceleration due to gravity, Δ is the temperature difference imposed between the lower and upper boundaries, L is the height of the fluid layer, and α , ν , and κ are properties of the fluid (thermal expansion coefficient, kinematic viscosity, and thermal diffusivity). The aspect ratio of the cell is the width of the cell divided by its height.
- [3] M. Sano, X.-Z. Wu, and A. Libchaber, *Phys. Rev. A* **40**, 6421 (1989).
- [4] B. Castaing, G. Gunaratne, F. Hetsch, L. P. Kadanoff, A. Libchaber, S. Thomae, X.-Z. Wu, S. Zaleski, and G. Zanetti, *J. Fluid Mech.* **204**, 1 (1989).
- [5] X.-Z. Wu, L. P. Kadanoff, A. Libchaber, and M. Sano, *Phys. Rev. Lett.* **64**, 2140 (1990).
- [6] G. Zocchi, E. Moses, and A. Libchaber, *Physica A* **166**, 387 (1990).
- [7] X.-Z. Wu and A. Libchaber, *Phys. Rev. A* **45**, 842 (1992).
- [8] Nu , the Nusselt number, is the ratio of the actual heat-transport rate mediated by the fluid to the rate which would be realized solely by conduction for the prescribed temperature difference. $Nu > 1$ when convection aids conduction in transporting heat.
- [9] X.-Z. Wu, B. Castaing, F. Hetsch, and A. Libchaber, in *Universalities in Condensed Matter*, edited by Remi Jul-
lien, Luca Peliti, Rammal Rammal, and Nino Boccara, Springer Proceeding in Physics Vol. 32 (Springer-Verlag, Berlin, 1988), p. 208.
- [10] W. V. R. Malkus, *Proc. R. Soc. London, Ser. A* **225**, 185 (1954); L. N. Howard, in *Proceedings of the 11th International Congress of Applied Mechanics, Munich, Germany*, edited by H. Gortler (Springer, Berlin, 1966), p. 1109.
- [11] E. E. DeLuca, J. Werne, R. Rosner, and F. Cattaneo, *Phys. Rev. Lett.* **64**, 2370 (1990).
- [12] J. Werne, E. E. DeLuca, R. Rosner, and F. Cattaneo, *Phys. Rev. Lett.* **67**, 3519 (1991).
- [13] B. I. Shraiman and E. D. Siggia, *Phys. Rev. A* **42**, 3650 (1990).
- [14] Z.-S. She, *Phys. Fluids A* **1**, 911 (1989).
- [15] V. Yakhot, *Phys. Rev. Lett.* **69**, 769 (1992).
- [16] The thermal boundary layers are regions with sharp temperature gradients adjacent to the top and bottom surfaces of the cell. These sharp thermal gradients exist because the heat flux enters and exits the cell solely by conduction due to the vanishing velocity on the boundaries.
- [17] S. Chandrasekhar, *Hydrodynamic and Hydromagnetic Stability* (Dover, New York, 1981).
- [18] The temperature and pressure in Eqs. (1) and (2) are related to their more conventional definitions (T', P') by the following: $T = (T' - T_0)/(\Delta/2)$ and $P = (P'/\rho + v^2/2 + gz')L^2/(4\kappa^2)$, where T_0 is the average of the temperatures to which the top and bottom boundaries of the fluid are held, ρ is the density of the fluid, and z' is the vertical distance measured from the mid-height between the upper and lower boundaries.
- [19] C. Canuto, M. Y. Hussaini, A. Quarteroni, and T. A. Zang, *Spectral Methods in Fluid Dynamics* (Springer-Verlag, New York, 1988).
- [20] L. Kleiser and U. Schumann, in *Proceedings of the Third Gesellschaft für Angewandte Mathematik und Mechanik Conference on Numerical Methods in Fluid Mechanics*, edited by E. H. Hirschel (Vieweg, Braunschweig, 1980), p. 165.
- [21] I. Goldhirsch, R. B. Pelz, and S. A. Orszag, *J. Fluid Mech.* **199**, 1 (1989).
- [22] A. N. Kolmogorov, *C. R. Dokl. Acad. Sci. URSS* **30**, 301 (1941).
- [23] W. D. Henshaw, H. O. Kreiss, and L. G. Reyna, *Theor. Comput. Fluid Dyn.* **1**, 65 (1989).
- [24] H. Tennekes and J. L. Lumley, *A First Course in Turbulence* (MIT, Cambridge, MA, 1972), p. 272.
- [25] G. K. Batchelor, *J. Fluid Mech.* **5**, 113 (1959).
- [26] E. W. Bolton, F. H. Busse, and R. M. Clever, *J. Fluid Mech.* **164**, 469 (1986).
- [27] It is predicted that the asymptotic scaling of Nu is $Ra^{1/2}$ [R. H. Kraichnan, *Phys. Fluids* **5**, 1374 (1962)]. In addition, a consequence of the detailed assumptions made by Shraiman and Siggia is that hard turbulence must be superseded by another flow regime at sufficiently high Ra .
- [28] M. B. Glauert, *J. Fluid Mech.* **1**, 625 (1956).
- [29] A. A. Townsend, *J. Fluid Mech.* **1**, 561 (1956).

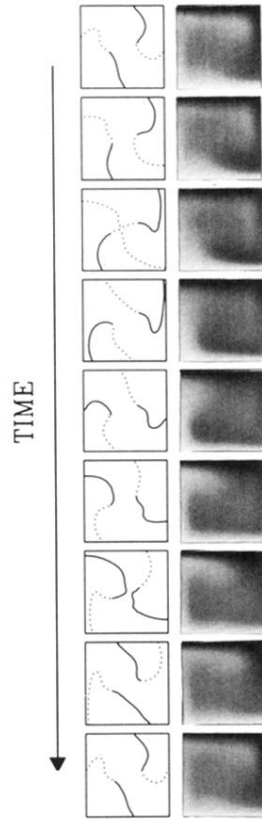


FIG. 1. Periodic convection with $Ra=8\times 10^4$ and $\sigma=7$. The sequence shows the evolution of the temperature field during one cycle. The right column depicts the temperature field; shades of gray are proportional to the temperature; white represents hot fluid. The left column shows two circulating waves which exist in the flow for this state. Solid lines represent hot “wave crests” while dashed lines depict cold “troughs.” Note the wave-wave interaction occurring in the third and seventh frames. The waves are visualized by plotting $\partial T/\partial t=0$ contours (i.e., contours of constant phase).

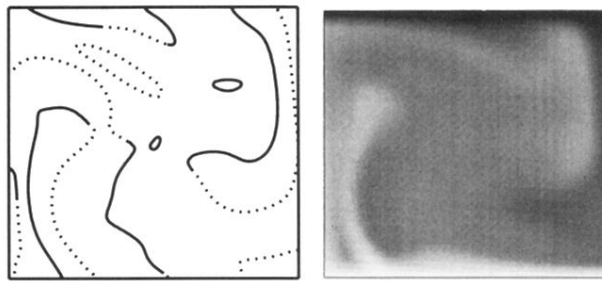


FIG. 2. Plume-dominated convection with $Ra=1.28 \times 10^6$ and $\sigma=7$. As in Fig. 1, on the left are cold (dashed) and hot (solid) $\partial T/\partial t=0$ contours while the temperature field is shown on the right. Thermal plumes grow from the thermal boundary layers and dominate the dynamics of the flow.

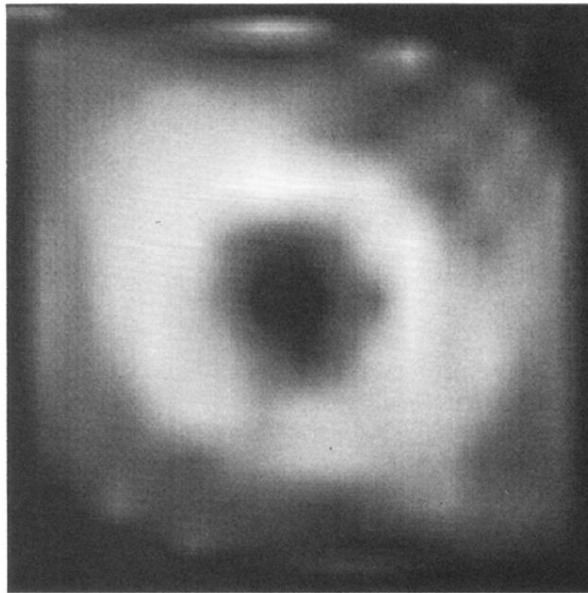


FIG 20. Signal-to-noise ratio of ω_p obtained with time traces of the temperature for $Ra=8.192 \times 10^7$ and $\sigma=7$. The prominent “ring” demarcates the path along which fluctuations are most pronounced. The figure is constructed using a coarse spatial subgrid (17×17 grid points) for 202 turnover times.

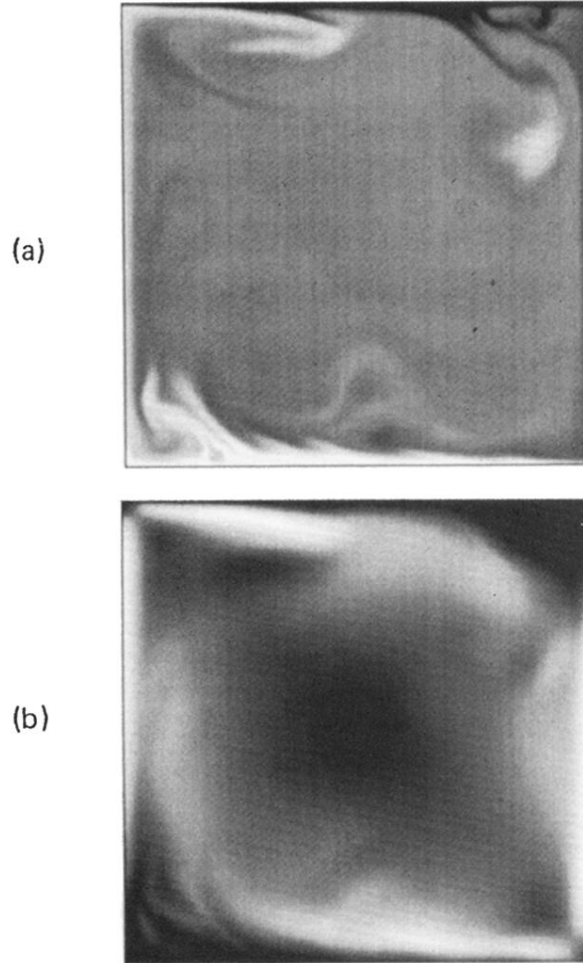


FIG. 3. Hard turbulence. $Ra=1.6384 \times 10^8$ and $\sigma=7$. (a) shows the fluid temperature. (b) depicts the magnitude of the velocity field with white representing high speeds. The maximum velocity for this snapshot is $11\,600(\kappa/L)$. The images relay the plume-roll interplay for hard turbulence: Plumes formed on the boundary layer do so in a strong wind resulting from the large-scale roll. The plumes are swept by the wind downstream where they coalesce to form a large plume. Large hot (cold) plumes, overcome by buoyancy, rise (fall) along the left (right) sidewall, driving the roll. When these large plumes impact the opposite boundary layer, they instigate the formation of other plumes [see top boundary of (a)] which continue the process.

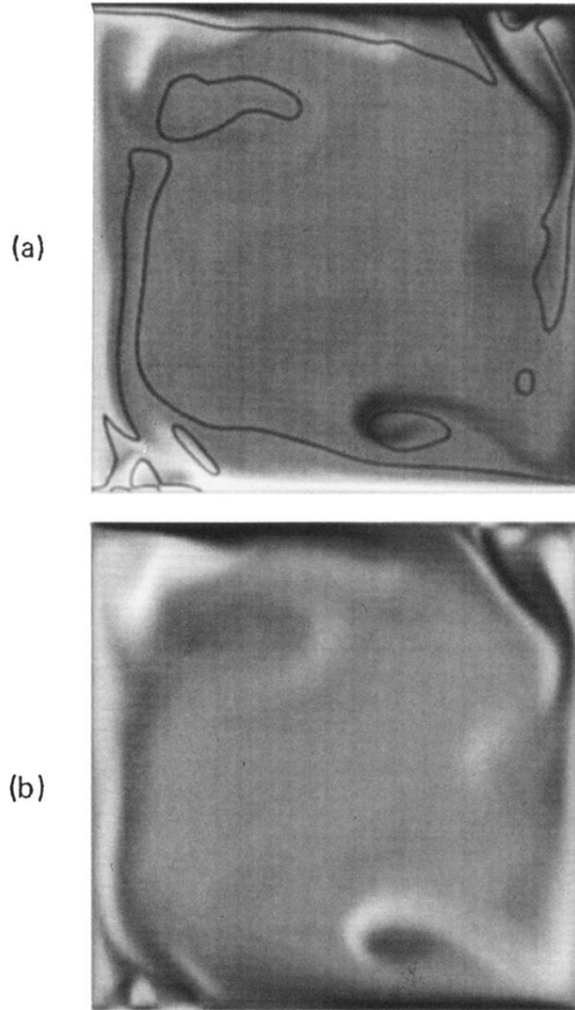


FIG. 7. The temperature (a) and the vorticity (b) for $Ra=8.192 \times 10^7$ and $\sigma=7$. Clockwise vorticity is shown as white. The contour for zero vorticity is superposed on the image of the temperature. The images demonstrate that newly formed plumes drive the large-scale circulation. The intense cold plume just emitted from the top boundary coincides with zero vorticity. Also, the sign of the vorticity indicates that the plume is forcing the fluid around it, rather than simply being dragged by the large-scale flow.

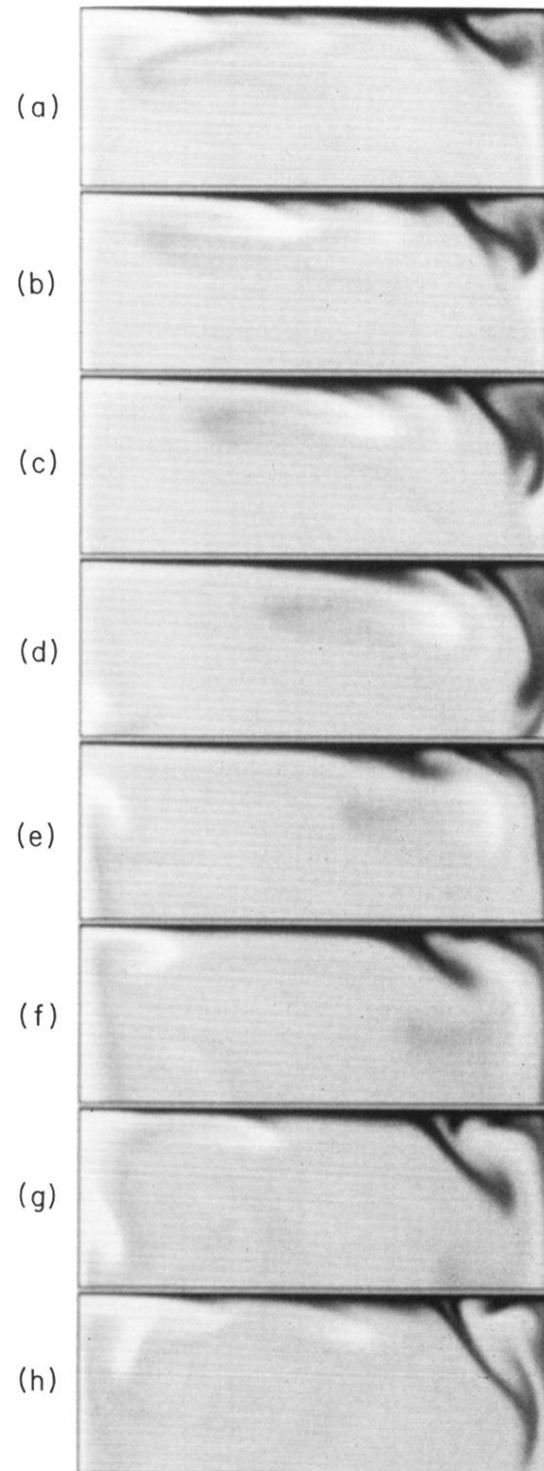


FIG. 8. Heat exchange between large hot plumes and the cold thermal boundary layer for $Ra=8.192 \times 10^7$ and $\sigma=7$. Each image shows the temperature field for the top 38% of the cell. (a)–(e) depict a hot plume as it sweeps across and exchanges heat with the cold boundary layer. (f)–(h) illustrate the coalescence of several cold plumes near the right corner.